Design and Bench Testing of a Model-Scale WEC for Advanced PTO Control Research

Giorgio Bacelli* Steven J. Spencer†, Ryan G. Coe*, Anirban Mazumdar†, David Patterson* and Kevin Dullea†
*Water Power Technologies Department,Sandia National Laboratories
Albuquerque, NM, USA
{gbacell, rcoe}@sandia.gov
†Robotics R&D Department, Sandia National Laboratories
Albuquerque, NM, USA
{sjspenc, amazumd, kjdulle}@sandia.gov

Abstract—Here, we discuss the design of a model-scale WEC for obtaining data to inform limitations of the simulations and provide better insight into control design and implementation for full scale systems. In addition to the design process for this device, we present a hardware load simulator for dry system performance and dynamics characterization. This load simulator system approximates the wave tank test environment, including linear inertia and stiffness, as well as some damping. This load simulator comprises the components of the classical spring-mass-damper system studied in many physics and system dynamics courses. By allowing the power take-off to excite the load simulator system, we are able to perform valuable bench testing experiments within the operating regimes that will be tested in the wave tank. Results from these bench tests and system identification show good performance from the actuator.

Index Terms—Dynamics characterization, High-torque brushless motors, Wave Energy Converter (WEC), Power Take-Off (PTO), Hardware-in-the-Loop Simulation

I. INTRODUCTION

Advanced control of the power take-off (PTO) in a wave energy converter (WEC) has shown significant promise for increasing wave energy absorption in simulation [1], [2]. While a large number of studies have considered numerical design and simulation of controllers for WECs, there has been a limited amount of research focused on the implementation of these controllers. For the implementation stage, it is essential to consider the design and testing of the actuator system through which a controller will function. Additionally, since the WEC is, in fact, a composite system which includes hydrodynamic, mechanical, electrical components, an accurate model of the PTO system is essential to optimal performance.

Model-scale testing of WECs is a complex and often expensive process. Sensors and data acquisition (DAQ) systems must be calibrated and verified. Additionally, actuators and real-time control systems (RCSs) must be tested and their performance must be assessed. Testing time within in a wave tank can amount to a significant portion of a project's budget. It is therefore desired that all possible pre-test work be completed before beginning testing in the wave tank.

Testing of an actuator and RCS is a task of particular importance. Beyond the need to perform a system checkout to verify proper function, it is often necessary to model the

TABLE I
MODEL-SCALE WEC PHYSICAL PARAMETERS.

Parameter	Value
Rigid-body mass (float & slider), m (kg)	858
Displaced volume, $\forall$ (m³)	0.858
Float radius, r (m)	0.88
Float draft, T (m)	0.53
Water density, ρ (kg/m³)	1000
Linear hydrostatic stiffness, G (kN/m)	25
Infinite-frequency added mass, A_∞ (kg)	822
Max vertical travel, $|z_{max}|$ (m)	0.6

dynamics and performance of the actuator system. This model is needed to design both low-level (i.e. basic force control) and high-level (i.e. to optimize performance) control algorithms. A particular challenge can arise in that to obtain an accurate model for the actuator system, it must operate in the same regime as will be used in wave tank testing. If, for example, the model-scale WEC weighs 500 kg, but system identification (SID) bench-testing uses only the moving mass of the drive train (e.g., 50 kg), the dynamic model obtained is likely to be quite different from that needed for wave tank testing.

II. SYSTEM DESIGN

A. Model-scale WEC

A 1/17th WEC device has been designed for tests concerned with the study of WEC modeling and control [3]. Fig. 1 and Table I show a diagram of the WEC device and its relevant physical parameters. A rendering from a CAD model of the system is shown in Fig. 3. Of particular interest for this paper are the linear hydrostatic stiffness, G, rigid-body mass, m, and infinite-frequency added mass, A_∞. These parameters were used to create a simplified approximation of the dynamics of the WEC device. Fig. 2 shows a photograph of the WEC device installed for testing in the Naval Surface Warfare Center, Carderock Division Maneuvering and Sea Keeping (MASK) Basin.

B. Actuators

The WEC is designed as a 3 degree freedom (DOF) machine, with actuators in heave, surge and pitch. Each of
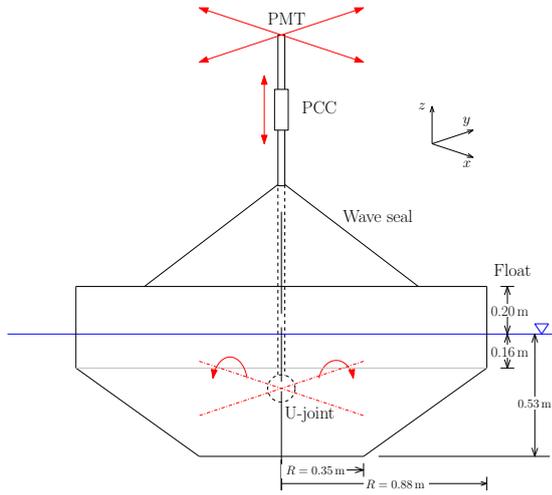
Fig. 1. Test device diagram.

Fig. 2. Test device installed in MASK basin.

the three stages is driven by a brushless three-phase permanent magnet direct current (PMDC) motor (Allied Motion MF0310100-C0X) with AMC DPEANIU-C100A400 motor controllers used for commutation and current control. Controllers are supplied by three-phase 208 VAC power. A 30 A outlet will be used for testing, allowing for a peak power draw of 10.8 kW. While the motors are capable of producing 1030 Nm of torque, the 100 A peak current output of the motor drives limits the produced torque to 636 Nm. Motor output torque is measured with Futek TRS300 (1 kNm rated load) rotary torque sensors.

The linear stages (heave and surge) are supported by PBC Linear IVT roller bearing carriages. Both of these stages have four carriages, each with a capacity of 10 kN. Belt drives,
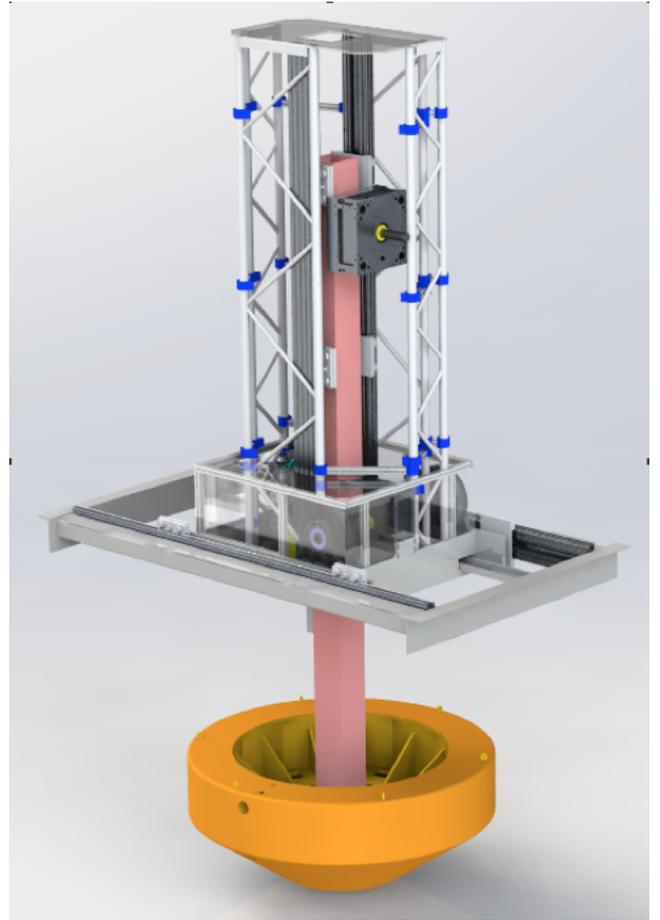

Fig. 3. CAD rendering of WEC device.

using 14 mm pitch Gates Polychain belts, perform the rotary to linear transmission. The tooth count on the heave and surge sprockets are 36 and 80 respectively. The actuation system can thus supply a peak force of 7.9 kN along the heave axis and 3.57 kN in surge. The belts are self-contained in a floating c-channel which is attached by a force transducer on one end to the structure, allowing for measurement of the force applied by the actuator. The heave stage uses a Futek LCB500 (13.3 kN rated load) load cell. The surge stage uses two Transducer Techniques LPO2K (8.9 kN rated load) load cells in parallel. The pitch axis transmission consists of two right angle gear heads and a shaft through the downtube connecting them. The gear ratios are 1:1 and 3:1 at the top and bottom of the shaft respectively. This allows for a peak torque of 1.9 kNm about the pitch axis which is measured with a Transducer Techniques TRS50K (5.65 kNm peak) at the output of the transmission.

Generated power is absorbed into the capacitors on the DC buses of the AMC controllers. If necessary, a built-in shunt regulator dumps excess power through an external 22 Ω 1 kW chassis mount shunt resistor (TE Connectivity TE1000B22RJ).

C. Data acquisition and real-time control

The WEC device is controlled through an EtherCAT network via Simulink Real-Time (SRT) running on a Speedgoat

Mobile real-time target machine and implemented from a development PC. The WEC control schemes are implemented in Simulink on the development machine. The Simulink model operates at a sampling frequency of 1 kHz on the SRT target. The target then sends commands and receives responses from the EtherCAT network as the EtherCAT master.

The EtherCAT network is composed of multiple modules, including the master and multiple slave modules. For this experimental setup, three motor controllers (intended for use in heave, surge and pitch actuation) are used on the network. The motor controllers serve to control the motors and read the motor feedback devices. They acquire absolute position at 10kHz from either Heidenhain ECN125 (heave) or ECN425 (pitch/surge) 25bits/revolution optical rotary encoders. The controllers take control information (desired current) from the SRT target and report measured current, position, and velocity of the motor back over the network. The position of the motors is then sent from the motor controllers back to the SRT target over the network.

The EtherCAT network also includes a set of DAQ slave modules, including three Beckhoff modules and a National Instruments (NI) module. The Beckhoff modules use a Beckhoff EK1100 coupler as the device communication port. The modules then have a set of terminals for reading and communicating with the sensors. The acquisition terminals include the following:

- Beckhoff EL3104 terminals for reading any voltage signals between ± 10 V
- Beckhoff EL3154 terminals for reading any current signals from 4 mA to 20 mA
- Beckhoff EL3356-0010 terminals for measuring in load cell and torque sensor values
- Beckhoff EL3692 terminals for measuring the resistance of motor thermistors
- Beckhoff EL4104 and EL4134 for analog outputs from 0-10 V and ± 10 V, respectively
- Beckhoff EL5001 terminals for communicating with the string potentiometers
- Beckhoff EL6001 for communicating with the Xsens MTi-20 IMU

The NI module includes an NI-9144 EtherCAT chassis to communicate with the network. The module contains a set of NI cRIO cards including an NI-9467 card to read a GPS timestamp, an NI-9225 card to read high voltages, 4 NI-9220 cards to read any ± 10 V inputs, and an NI-9401 to send and read digital inputs and outputs.

The EtherCAT network uses standard Ethernet cables and the EtherCAT communication protocol developed by Beckhoff and standardized in IEC 61158. The system is then distributed with different individual modules throughout the WEC device to avoid long analog and high voltage signal runs The EtherCAT system will be synchronized with the use of the distributed clock functionality of the EtherCAT protocol. The distributed clock (DC) synchronization algorithm determines the delay of the signal from one module to the next and from terminal to terminal within each module. The algorithm
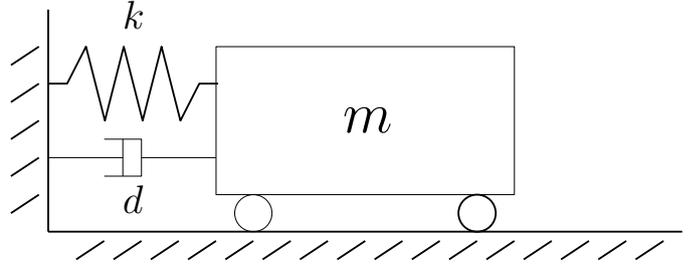

Fig. 4. Simple spring-mass-damper system.

also precisely aligns the clock time stored on each module and terminal. Once the delays are known and the clocks are aligned, the system can synchronize the DC to within tens of nanoseconds, ensuring very accurate and synchronized measurements [4].

D. Dynamics simulator

Using commercially-available off-the-shelf (COTS) parts, a spring-mass-damper system was designed to match the parameters of the WEC device given in Table I. Physics and dynamics books often consider a wide variety of spring-mass-damper systems. The most simple system is depicted in Fig. 4. Physical implementation of this system, especially at large scale, is not so trivial. In general, large scale springs are designed to work well only in either compression or extension, not both. Thus, to provide a spring reaction, a number of systems were considered. Air-fluid accumulators, in which air is compressed by a hydraulic system, were first identified as a potential option, but later ruled out because of high costs of the large components required. A number of systems in which hydraulic gearing would be used to reduce overall travel distances were also considered, but were avoided due to additional complexity.

Large "coil-over" springs, which are designed for use in off-road vehicle suspensions, were identified as a potential solution. These springs can have sufficient stiffness and travel on the order of 0.5 m. In their intended use, coil-over springs work only in compression as they are pre-loaded by the weight the of the vehicle. After confirming from a manufacturer that it would be best to avoid using the springs with significant tension loads, the opposing spring system shown in Fig. 5 was selected. To make the best use of COTS parts and reduce the chance of buckling, compound springs were selected, comprising two springs in series.

The individual springs have a stiffness of k_A. When placed in series, each compound spring has a stiffness of k_B.

$$\frac{1}{k_B} = \frac{1}{k_A} + \frac{1}{k_A} \tag{1a}$$

$$k_B = \frac{1}{2} k_A \tag{1b}$$

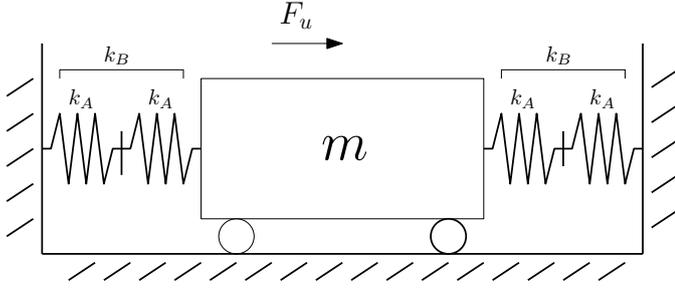Placement of the compound springs on opposing sides of the mass puts them in parallel with each other; resulting in an
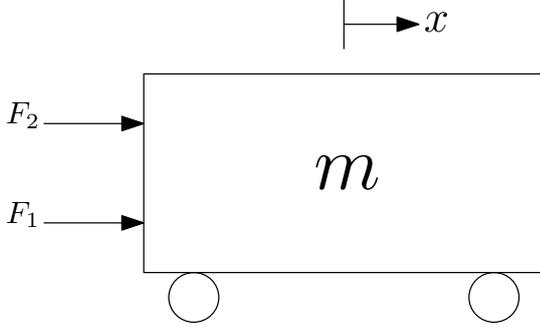
Fig. 5. WEC dynamics simulator system diagram.

Fig. 6. WEC dynamics simulator free-body-diagram.

Fig. 7. Force plot for opposing spring system.

effective stiffness for the system of $2k_B$ or more simply k_A. A free body diagram of the system is depicted in Fig. 6. At $x = 0$, F_1 and F_2 completely offset each other and the sum of the forces on the system is zero. As the cart moves to the right, the magnitude of F_1 decreases and magnitude of F_2 increases. The relationship, as relating the to diagram in Fig. 6, is shown in Fig. 7. Thus a simplified equation of motion for the cart is

$$m\ddot{x} + k_A x = F_a, \qquad (2)$$

where F_a is any external actuator forcing. Thus from, (1) and (2), a COTS spring with $k_A = G = 25$ kN/m ($\sim$ 143lbf/in) is desired. To insure that the springs act only in compression, they must be compressed to half their total travel. Since each of the opposing compound springs is composed of two springs in series, the max travel of each individual spring should be chosen equal to $|z_{max}|$.

The fully assembled test-rig and actuator system is shown in Fig. 8. The actuator system (on the left) is coupled to the test-rig (on the right) via a dual ball joint. The entire system is also coupled together via two large angle iron members that run along the floor.

III. SYSTEM IDENTIFICATION (SID)

The objective of these bench testing experiments is to characterize the dynamic response of the heave actuator system and test-rig. The results of this characterization will be used to design and test control systems prior to wave tank testing. The input to the system is the desired force generated by the actuator. This process follows a design of experiments similar to that used in [5]. To perform the modeling of the system, a
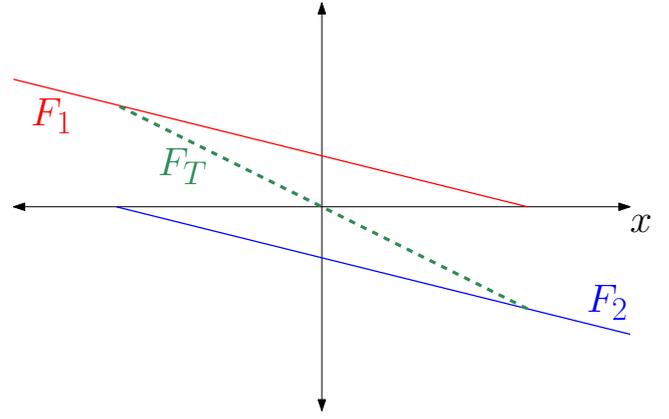
band-limited white noise input signal is utilized. Fig. 9 shows the power spectrum for input signal used to perform a SID analysis on the actuator test system. This signal was input as the commanded force. In order to characterize and understand the actuator for control system design, a number of response functions have been estimated.

Fig. 10 shows the estimated frequency response function (FRF) between commanded torque (τ_c) and measured torque (τ). This function describes how well the motor responds to desired commands. Flat responses up to 10 Hz, with a magnitude of 0 dB and a phase very close to 0 deg, show that the motor responds accurately within the desired region.

Fig. 11 shows the estimated FRF between measured torque (τ) and rotational velocity (ω). This function shows the dynamics of the physical system. We can clearly see that the system has resonances at 0.8, 30, and 40 Hz. The 0.8 Hz resonance is created by the spring-mass-damper test-rig system described above, and closely matches that of the 1/17-scale WEC device. To verify that the peak in the response at 0.8 Hz corresponds to the mass-spring system it is possible to use the formula $f_{res} = 0.75$ Hz, where $m = 1060$ kg is the mass and $k = 23.5$ kN/m is the spring coefficient. The higher frequency resonances at 30 and 40 Hz is likely from the Kevlar belt in the actuators drivetrain having non-negligible compliance.

Additional insight can be gained from developing a first principles based model for the entire system. A linear model of the combined actuator/load system is shown in Fig. 12. For simplicity we allow the representation of the motor to be in the translational frame with forces and velocities converted by the transmission ratio and the reflected inertia and damping converted by the square of the ratio. The stiffness and damping of the belt (k_b and c_b respectively) transmit force from the actuator to the load and take the role of F_a from (2). We do, however, improve the prior model of the load by introducing damping to the load such that the resonant peak will be finite.

This system has one input.

$$u_{heave} = \begin{bmatrix} F_m \end{bmatrix} \qquad (3)$$
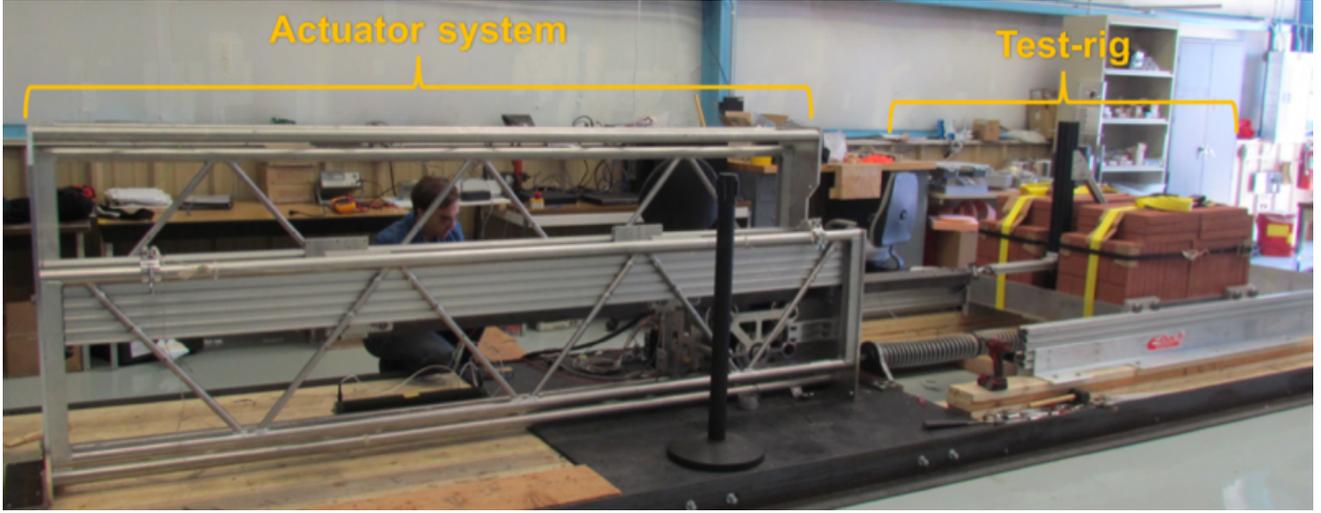
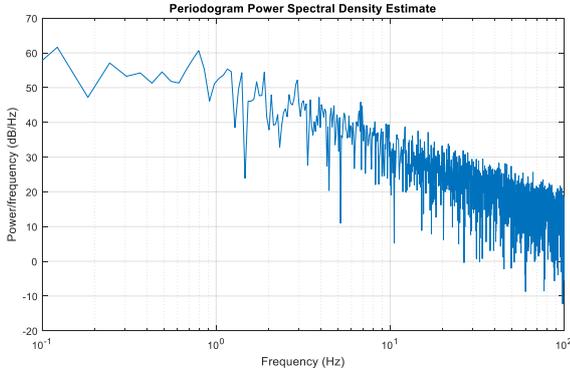Fig. 8. Photograph of assembled actuator and test-rig system.

Fig. 9. Input signal for system identification of actuator test system.

Here, F_m is the motor force (converted to the linear frame). We consider five measured outputs.

$$y_{heave} = \begin{bmatrix} x_m \\ x_l \\ \dot{x}_m \\ F_a \\ F_m \end{bmatrix} \qquad (4)$$

The applied force is F_a. The motor position and velocity in the linear frame are x_m and $\dot{x}_m$ respectively. The position of the load is given by x_l. We can represent this system with four states

$$x_{heave} = \begin{bmatrix} x_m \\ x_l \\ \dot{x}_m \\ \dot{x}_l \end{bmatrix}, \qquad (5)$$

where $\dot{x}_l$ is the load velocity, and get the following state-space model.

$$A_{heave} = \begin{bmatrix} 0_2 & I_2 \\ M^{-1}K & M^{-1}\mathcal{C} \end{bmatrix} \quad B_{heave} = \begin{bmatrix} 0 \\ 0 \\ \frac{1}{m_m} \\ 0 \end{bmatrix}$$

$$C_{heave} = \begin{bmatrix} 1 & 0 & 0 & 0 \\ 0 & 1 & 0 & 0 \\ 0 & 0 & 1 & 0 \\ -k_b & k_b & c_b & -c_b \\ 0 & 0 & 0 & 0 \end{bmatrix} \quad D_{heave} = \begin{bmatrix} 0 \\ 0 \\ 0 \\ 0 \\ 1 \end{bmatrix} \qquad (6)$$

Here, m_m is the inertia of the motor in the linear frame. The belt stiffness and damping are k_b and c_b respectively. The matrices M, K, and $\mathcal{C}$ are defined as follows.

$$M = \begin{bmatrix} J_m N^2 & 0 \\ 0 & m_l \end{bmatrix} = \begin{bmatrix} m_m & 0 \\ 0 & m_l \end{bmatrix} \qquad (7)$$

$$K = \begin{bmatrix} -k_b & k_b \\ k_b & -k_b - k_l \end{bmatrix} \qquad (8)$$

$$\mathcal{C} = \begin{bmatrix} c_b - c_m & c_b \\ c_b & -c_b - c_l \end{bmatrix} \qquad (9)$$

In (7), J_m is the motor rotational inertia and N is the transmission ratio of the belt drive. The stiffness, mass and damping of the spring-mass-damper subsystem are k_l, m_l and c_l respectively. The motor damping is c_m.

While high performing, our motor and controller does not provide perfectly controlled force source. We can model this as well as standard DC motor with PI control in the non-invariant DQ frame. We model it with two inputs since connecting this to our actuator/load system will create a feedback where developed motor velocity produces a back EMF: desired force, F_{des}, and motor velocity (converted to the linear frame), $\dot{x}_m$.
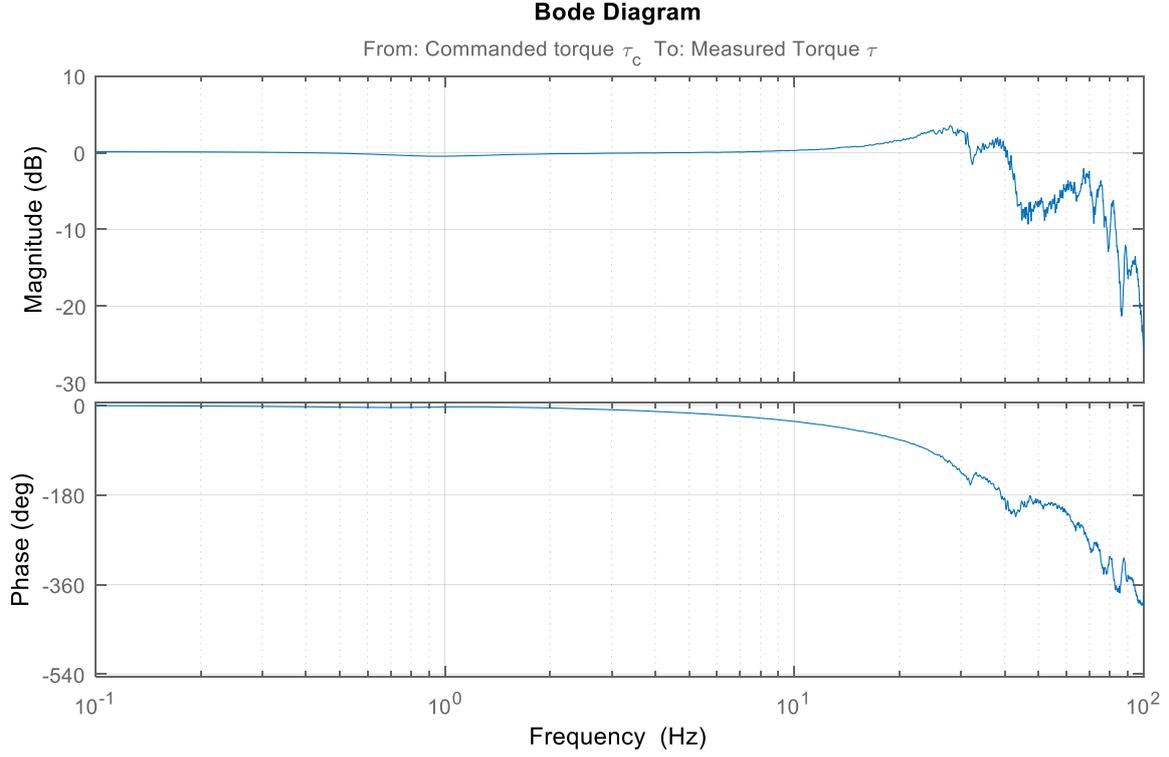
Bode Diagram

From: Commanded torque τ_c To: Measured Torque τ

Fig. 10. Estimated FRF between commanded torque (τ_c) and measured torque (τ).

$$u_{F_m} = \begin{bmatrix} F_{\text{des}} \\ \dot{x}_m \end{bmatrix} \tag{10}$$

We only care about one output for this system

$$y_{F_m} = \begin{bmatrix} F_m \end{bmatrix} \tag{11}$$

Because of the PI controller we need two states, the actual quadrature current (i_q) and the integral of the measured error ($\int e$).

$$x_{F_m} = \begin{bmatrix} i_q \\ \int e \end{bmatrix} \tag{12}$$

This yields the system to described the motor subsystem.

$$A_{F_m} = \begin{bmatrix} \frac{-(R+K_p)}{L} & \frac{-K_i}{L} \\ 1 & 0 \end{bmatrix} \quad B_{F_m} = \begin{bmatrix} \frac{K_p}{L}\frac{1}{NK_t} & -\frac{1}{L}K_\omega N \\ -\frac{1}{NK_t} & 0 \end{bmatrix}$$

$$C_{F_m} = \begin{bmatrix} NK_t & 0 \end{bmatrix} \quad D_{F_m} = \begin{bmatrix} 0 & 0 \end{bmatrix} \tag{13}$$

Here, R and L are the phase-neutral resistance and inductance of the motor respectively, K_p and K_i are the proportional and integral feedback constants of the PI controller respectively, K_t and K_w are torque and back EFM constants of the motor.

Finally, we can connect the systems from (6) and (13) to get a linear model the full system.

$$u_{sys} = \begin{bmatrix} F_{\text{des}} \end{bmatrix} \quad y_{sys} = \begin{bmatrix} x_m \\ x_l \\ F_a \\ F_m \end{bmatrix} \quad x_{sys} = \begin{bmatrix} i_q \\ \int e \\ x_m \\ x_l \\ \dot{x}_m \\ \dot{x}_l \end{bmatrix}$$

$$A_{sys} = \begin{bmatrix} A_{F_m} & \begin{matrix} 0 & 0 & \frac{1}{L}K_\omega N & 0 \\ 0 & 0 & 0 & 0 \end{matrix} \\ \begin{matrix} 0 & 0 \\ 0 & 0 \\ \frac{K_t N}{m_m} & 0 \\ 0 & 0 \end{matrix} & A_{heave} \end{bmatrix} \tag{14}$$

$$B_{sys} = \begin{bmatrix} \frac{K_p}{L}\frac{1}{NK_t} \\ -K_t N \\ 0_{4\times1} \end{bmatrix}$$

$$C_{sys} = \begin{bmatrix} 0 & 0 & 1 & 0 & 0 & 0 \\ 0 & 0 & 0 & 1 & 0 & 0 \\ 0 & 0 & 0 & 0 & 1 & 0 \\ 0 & 0 & -k_b & k_b & c_b & -c_b \\ K_t N & 0 & 0 & 0 & 0 & 0 \end{bmatrix}$$

$$D_{sys} = 0_{5\times1}$$

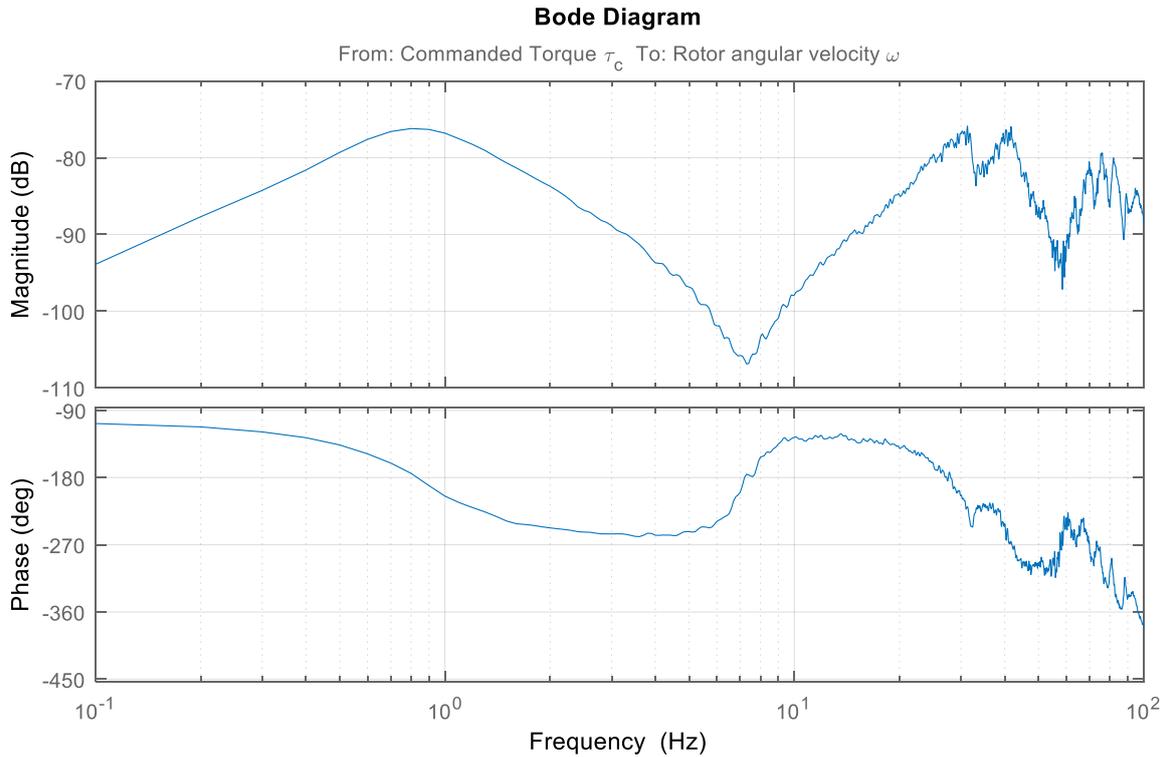The resulting frequency response of this system versus the system ID data can be seen in Figures 13 and 14.

Bode Diagram

From: Commanded Torque τ_c To: Rotor angular velocity ω

Fig. 11. Estimated FRF between measured torque (τ) and rotational velocity (ω).

$$x_m = \frac{\theta_m}{N}$$

$$x_l$$

$$k_b$$

$$k_l$$

$$F_m = \tau_m N$$

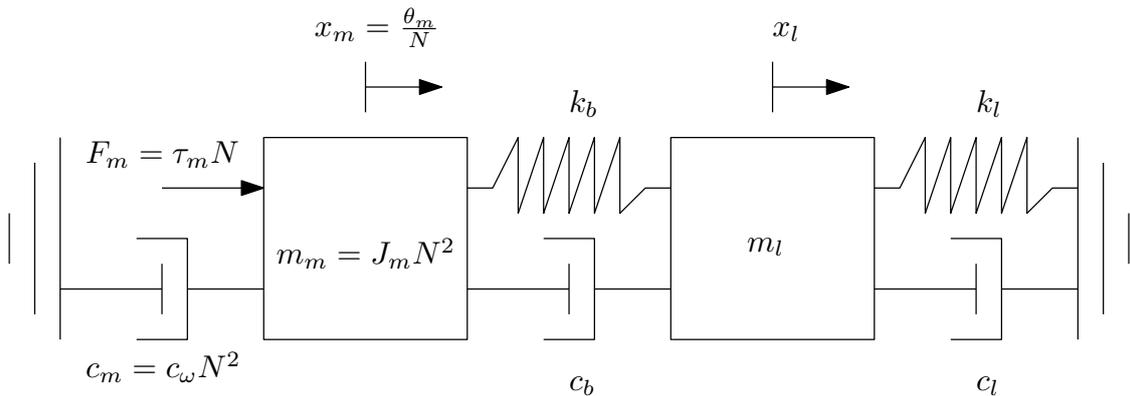$$m_m = J_m N^2$$

$$m_l$$

$$c_m = c_\omega N^2$$

$$c_b$$

$$c_l$$

Fig. 12. Actuation/load system diagram.

IV. CONCLUSIONS

An actuator system was designed and assembled for a 1/17-scale WEC. Three separate actuation systems for heave, surge, and pitch were developed. A test-rig was constructed to perform dry bench testing of the heave actuator system before wave tank testing. This system simulates the dynamics of the 1/17-scale WEC to be used in wave tank testing. SID experiments and subsequent analysis show that the actuator system performs as designed. The actuator provides an accurate response up to roughly 10 Hz. An analytic approach to produce a parametric model of the actuator shows that the system is operating as designed.

Future work with this system will be performed to study real-time closed-loop control implementation. The test-rig described here will be used for development and testing of real-time controllers. Subsequently, the system and controllers will be used in model scale wave tank testing. WEC PTOs must operate in a manner that is quite different from most generator systems. While other systems (e.g., for wind, coal, nuclear) use generators which operate a relatively steady set-point, most
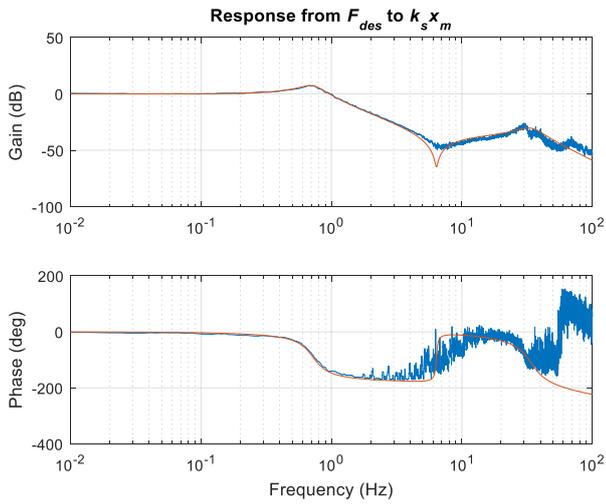
Fig. 13. Desired force (F_{des}) to position (x). Position is scaled by k_s to provide $0\,\text{dB}$ gain at low frequency.
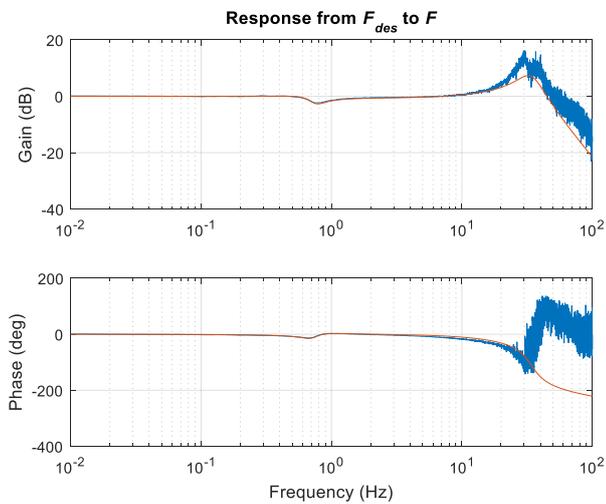

Fig. 14. Desired force (F_{des}) to actuator force (F_a). Model captures dip in gain around the load resonance. Also predicts high frequency resonance.

WECs produce oscillatory mechanical energy. Thus, a more in-depth study should be conducted to better understand optimal design for WEC PTO systems.

REFERENCES

[1] J. Hals, J. Falnes, and T. Moan, "A comparison of selected strategies for adaptive control of wave energy converters," *Journal of Offshore Mechanics and Arctic Engineering*, vol. 133, no. 3, p. 031101, March 2011. [Online]. Available: http://offshoremechanics.asmedigitalcollection.asme.org/article.aspx?articleid=1456895

[2] D. Wilson, G. Bacelli, R. G. Coe, D. L. Bull, O. Abdelkhalik, U. A. Korde, and R. D. Robinett III, "A comparison of WEC control strategies," Sandia National Labs, Albuquerque, New Mexico, Tech. Rep. SAND2016-4293, April 2016 2016.

[3] R. G. Coe, G. Bacelli, D. Patterson, and D. G. Wilson, "Advanced WEC Dynamics & Controls FY16 testing report," Sandia National Labs, Albuquerque, NM, Tech. Rep. SAND2016-10094, October 2016. [Online]. Available: https://mhkdr.openei.org/submissions/151

[4] G. Cena, I. C. Bertolotti, S. Scanzio, A. Valenzano, and C. Zunino, "Synchronize your watches: Part ii: Special-purpose solutions for distributed real-time control," *IEEE Industrial Electronics Magazine*, vol. 7, no. 2, pp. 27–39, June 2013.

[5] G. Bacelli, R. G. Coe, D. Patterson, and D. Wilson, "System identification of a heaving point absorber: Design of experiment and device modeling," *Energies*, vol. 10, no. 10, p. 472, 2017. [Online]. Available: http://www.mdpi.com/1996-1073/10/4/472